Numerical simulation of a rising bubble under the influence of electric forces using ISPH method

A. Rahmat[a,d], M. Yildiz[a,b,c,*]

[a] *Faculty of Engineering and Natural Sciences, Sabanci University, Tuzla, 34956 Istanbul, Turkey*
[b] *Integrated Manufacturing Technologies Research and Application Center, Sabanci University, Tuzla, 34956, Istanbul, Turkey*
[c] *Composite Technologies Center of Excellence, Sabanci University-Kordsa, Istanbul Technology Development Zone, Sanayi Mah. Teknopark Blvd. No: 1/1B, Pendik, 34906 Istanbul, Turkey*
[d] *School of Chemical Engineering, University of Birmingham, Edgbaston Birmingham, B15 2TT, United Kingdom*

Abstract

The motion of a single rising bubble is simulated under the effect of electric forces using the ISPH method. In order to model interfacial forces on bubble surface, a diffusive interface with a finite thickness is employed. Using the leaky dielectric model, the electric forces act on the bubble interface and change the topology of the rising bubble, in competence with other interfacial and volumetric forces. The influence of the applied electric field on a rising bubble is investigated for an oil-water system with realistic density and viscosity ratios. Then, the effect of interfacial forces on the bubble shape and flow behaviour will be illustrated in variations of Electro-capillary (Ec) and Bond (Bo) numbers.

Keywords: Smoothed Particle Hydrodynamics, Multiphase flows, Bubble dynamics, Electrohydrodynamics (EHD)

1. Introduction

Bubble/droplet rising is one of the branches of multiphase flows that considers the rising motion of a lighter dispersed phase (droplet phase) in a heavier continuous phase of another liquid mainly due to the buoyancy force. Bubble rising has been observed in numerous natural phenomena and industrial applications. Nucleate pool boiling [1], oil in water (o/w) and water in oil (w/o) emulsions used in manufacturing of products in the food, pharmaceutical, cosmetic, and paint industries [2, 3] and separation of oil-water emulsions in petroleum refineries and waste-water treatment industry [4, 5], as well as chemical reactions [6] are among industrial practices where droplet rising is frequently observed.

To investigate droplet rising, studies have been carried out to determine the droplet regimes for different sets of hydrodynamic properties. Clift *et al.* [7] reviewed the phenomenon and illustrated that the droplet regimes can be categorized by three dimensionless numbers, namely the Reynolds, Morton, and Eotvos numbers. Nonetheless, other parameters may also influence the droplet rising regime. In order to control the droplet rising conditions and maintain the preferable flow regime and rising characteristics, various techniques have been examined in the literature. Investigated both numerically [8, 9] and experimentally [10, 11], adding surfactants to the multi-phase system can adjust the surface tension to a desired value, resulting in proper control of the droplet rising regimes. However, limitations such as their serious impacts on human-being and animal lives [12, 13] restricts their usage in multi-phase flow systems. Alternatively, the utilization of electric forces is another feasible solution for controlling the droplet rising phenomenon. Yet, the electrohydrodynamic effects on the rising droplet have not been fully discovered.

*Corresponding author
Email address: meyildiz@sabanciuniv.edu (M. Yildiz)

The influence of electrohydrodynamic (EHD) forces is successfully implemented to some of the droplet dynamic problems such as droplet deformation. In order to implement the EHD forces, the leaky dielectric model was introduced [14] which presumes a finite electrical conductivity for fluids resulting in accumulation of electric charges on the interface. The electric charges induce tangential forces leading to both prolate and oblate deformations depending on electric permittivity and conductivity ratios. Mahlmann *et al.* [15] carried out a two-dimensional simulation of a gas droplet rising in a viscous fluid under the perfect dielectric assumption. They investigated the deformation of a rising droplet for variations of electric field strength, surface tension and viscosity. They revealed that the droplet initially deforms into a prolate shape and later flattens into an oblate one thereby experiencing "wobbly-like" oscillations. Finally, Yang *et al.* [16] studied the droplet rising under horizontal and vertical electric fields using a perfect dielectric model, numerically. They showed that vertical electric field enhance the rising motion of the droplet while the horizontal electric field hinders the rising motion.

The Smoothed Particle Hydrodynamics (SPH) method is chosen to simulate the problem. The method was initially developed by Gingold and Monaghan [17] for astrophysical purposes. However, the method is employed for the simulation of a broad range of physical applications, namely, free-surface flows [18, 19], multi-phase flows [20–22], and fluid-solid interactions [23, 24], among others. In the SPH method, the domain is discretized with fluid particles having physical properties such as density and viscosity. The physical values are averaged and smoothed over fluid particles by means of a kernel function based on the distance between the particle of interest and its neighboring particles. The interface between fluid phases is determined by means of a color function being averaged over particles. Here, it is shown that the SPH method is capable of modeling multiphase problems such as droplet rising under the influence of external electric field.

In this paper, the rising of a liquid droplet in another liquid is numerically investigated under the influence of EHD forces for various dimensionless numbers. In §2, the governing equations for a two-phase incompressible system are introduced along with the relevant dimensionless parameters and ratios. The effect of the electric field on the flow is implemented using the leaky dielectric model. In §3, the SPH method and the numerical scheme are concisely presented. In §4, the problem setup and boundary conditions for the computational domain are given, and the in-house code is validated with the available data in literature and the particle resolution study is performed. In §5, the results are presented and detailed discussions are provided for variations of electrical Capillary and Bond numbers. Finally, concluding remarks are drawn in §6.

2. Governing equations

Equations governing an incompressible flow may be written as

$$\boldsymbol{\nabla} \cdot \mathbf{u} = 0, \tag{1}$$

$$\rho \frac{\mathrm{D}\mathbf{u}}{\mathrm{D}t} = -\boldsymbol{\nabla} p + \frac{1}{\mathrm{Re}} \boldsymbol{\nabla} \cdot \boldsymbol{\tau} + \frac{1}{\mathrm{Bo}} \mathbf{f}_{(s)} + \frac{1}{\mathrm{Eg}} \mathbf{f}_{(e)}, \tag{2}$$

where $\mathbf{u}$ is the velocity vector, p is pressure, ρ is density, t is time and $\mathrm{D}/\mathrm{D}t = \partial/\partial t + \mathbf{u} \cdot \boldsymbol{\nabla}$ represents the material time derivative. Here, $\boldsymbol{\tau}$ is the viscous stress tensor,

$$\boldsymbol{\tau} = \mu \left[\boldsymbol{\nabla}\mathbf{u} + (\boldsymbol{\nabla}\mathbf{u})^{\dagger} \right], \tag{3}$$

where μ denotes viscosity and superscript $\square^{\dagger}$ represents the transpose operation. Local surface tension force is expressed as an equivalent volumetric force according to the continuum surface (CSF) method [25],

$$\mathbf{f}_{(s)} = \gamma \kappa \hat{\mathbf{n}} \delta. \tag{4}$$

Here, surface tension coefficient, γ, is taken to be constant while κ represents interface curvature, $-\boldsymbol{\nabla} \cdot \hat{\mathbf{n}}$, where $\hat{\mathbf{n}}$ is unit surface normal vector. $\mathbf{f}_{(e)}$ is the electric force vector defined as [26]

$$\mathbf{f}_{(e)} = -\frac{1}{2} \mathbf{E} \cdot \mathbf{E} \boldsymbol{\nabla} \varepsilon + q^{v} \mathbf{E}. \tag{5}$$

In the above equation, ε denotes electric permittivity, q^v is the volume charge density near the interface while $\mathbf{E}$ is the electric field vector. Assuming small dynamic currents and neglecting magnetic induction effects, the electric field is irrotational [27] and may be represented by gradient of an electric potential ϕ, $\mathbf{E} = -\boldsymbol{\nabla}\phi$. Further assumption of fast electric relaxation time compared to viscous relaxation time leads to the following relations for electric potential and charge density

$$\boldsymbol{\nabla} \cdot (\sigma \boldsymbol{\nabla}\phi) = 0, \tag{6}$$

$$q^v = \boldsymbol{\nabla} \cdot (\varepsilon \boldsymbol{\nabla}\phi), \tag{7}$$

where σ is the electrical conductivity.

Dimensionless values are formed using the following scales

$$\begin{aligned} &\mathbf{x} = \mathbf{x}^+/r, \quad \rho = \rho^+/\rho_f, \quad \mu = \mu^+/\mu_f \quad \mathbf{u} = \mathbf{u}^+/\sqrt{gr}, \\ &t = t^+\sqrt{g/r}, \quad \mathbf{E} = \mathbf{E}^+/E_\infty, \quad p = \left(p^+ - \rho \mathbf{g}\cdot\mathbf{x}^+\right)/\rho_f g r, \\ &\mathcal{D} = \rho_d/\rho_f, \quad \mathcal{V} = \mu_d/\mu_f, \quad \mathcal{P} = \varepsilon_d/\varepsilon_f, \quad \mathcal{C} = \sigma_d/\sigma_f, \end{aligned} \tag{8}$$

leading to Reynolds, Bond, Electro-gravitational and electrical Capillary numbers defined as

$$\mathrm{Re} = \frac{\rho_f\sqrt{gr^3}}{\mu_f}, \quad \mathrm{Bo} = \frac{\rho_f g r^2}{\gamma}, \quad \mathrm{Eg} = \frac{\rho_f g r}{\varepsilon_f E_\infty^2}, \quad \mathrm{Ec} = \frac{\mathrm{Bo}}{\mathrm{Eg}}. \tag{9}$$

Here r is the droplet radius, E_∞ is the undisturbed electric field intensity and g is the gravitational acceleration. A plus sign marks dimensional variables whereas subscripts $\square_d$ and $\square_f$ denote droplet and background fluid phases, respectively.

3. Numerical method

To distinguish between different phases, a color function $\hat{c}$ is defined such that it assumes a value of zero for one phase and unity for the other. The color function is then smoothed out across the phase boundaries as

$$c_\mathrm{i} = \sum_{\mathrm{j}=1}^{J_n} \frac{\hat{c}_\mathrm{j} W_\mathrm{ij}}{\psi_\mathrm{i}}, \tag{10}$$

to ensure smooth transition between the properties of each phase when used for their interpolation. Here, $\psi_\mathrm{i} = \sum_{\mathrm{j}=1}^{J_n} W_\mathrm{ij}$, is the number density of SPH particle i, calculated as the sum of the interpolation kernel of neighboring particles i and j over all neighbors of particle i, J_n. The interpolation kernel $W(r_\mathrm{ij}, h)$, concisely noted as W_ij, is a function of the magnitude of distance vector, $\mathbf{r}_\mathrm{ij} = \mathbf{r}_\mathrm{i} - \mathbf{r}_\mathrm{j}$, between particle of interest i and its neighboring particles j and h, the smoothing length [28, 29]. Interpolation of phase properties is carried out using Weighted Arithmetic Mean (WAM),

$$\chi_\mathrm{i} = c_\mathrm{i}\chi_d + (1 - c_\mathrm{i})\,\chi_f, \tag{11}$$

where χ may denote density, viscosity, permittivity or conductivity of the fluids. The smoothed color function is also utilized to evaluate $\delta \simeq |\boldsymbol{\nabla} c|$, $\kappa = -\boldsymbol{\nabla}\cdot\hat{\mathbf{n}}$ and $\hat{\mathbf{n}} = \boldsymbol{\nabla} c/|\boldsymbol{\nabla} c|$ in equation (4). In this formulation, a constraint has to be enforced to avoid possible erroneous normals [30]. In this study, only gradient values exceeding a certain threshold, $|\boldsymbol{\nabla} c_\mathbf{i}| \simeq \alpha/h$, are used in surface tension force calculations. A α value of 0.08 has been found to provide accurate results without removing too much detail [31].

A predictor-correcter scheme is employed to advance the governing equations of flow in time using a first-order Euler approach with variable timestep according to Courant-Friedrichs-Lewy condition, $\Delta t = \zeta h/u_\mathrm{max}$, where u_max is the largest particle velocity magnitude and ζ is taken to be equal to 0.25 [31]. In predictor step all the variables are advanced to their intermediate form using following relations,

$$\mathbf{r}_\mathrm{i}^* = \mathbf{r}_\mathrm{i}^{(n)} + \mathbf{u}_\mathrm{i}^{(n)}\Delta t + \boldsymbol{\delta}\mathbf{r}_\mathrm{i}^{(n)}, \tag{12}$$

$$\mathbf{u}_{\mathrm{i}}^{*} = \mathbf{u}_{\mathrm{i}}^{(n)} + \frac{1}{\rho_{\mathrm{i}}^{(n)}} \left(\frac{1}{\mathrm{Re}} \boldsymbol{\nabla} \cdot \boldsymbol{\tau}_{\mathrm{i}} + \frac{1}{\mathrm{Bo}} \mathbf{f}_{(s)\mathrm{i}} + \frac{1}{\mathrm{Eg}} \mathbf{f}_{(e)\mathrm{i}} \right)^{(n)} \Delta t, \tag{13}$$

$$\psi_{\mathrm{i}}^{*} = \sum_{\mathrm{j}=1}^{J_n} W_{\mathrm{ij}}^{*}, \tag{14}$$

where starred variables represent intermediate values and superscript (n) denotes values at the nth time step. Artificial particle displacement vector in (12) is implemented through $\boldsymbol{\delta}\mathbf{r}_{\mathrm{i}}^{(n)}$ as

$$\boldsymbol{\delta}\mathbf{r}_{\mathrm{i}}^{(n)} = \beta \left[u_{\max} \sum_{\mathrm{j}=1}^{J_n} \left(\frac{\mathbf{r}_{\mathrm{ij}}}{r_{\mathrm{ij}}^{3}} r_{\mathrm{avg,i}}^{2} \right) \right]^{(n)} \Delta t, \tag{15}$$

which ensures orderly particle distribution. Average particle spacing is found via $r_{\mathrm{avg,i}} = \sum_{\mathrm{j}=1}^{J_n} r_{\mathrm{ij}}/J_n$ while a value of $\beta = 0.06$ is employed throughout this study [32].

Using intermediate values, pressure at the next time step is found by solving the Poisson equation which is then followed by corrections in position and velocity of the particles, completing the temporal transition.

$$\nabla \cdot \left(\frac{1}{\rho_{\mathrm{i}}^{*}} \boldsymbol{\nabla} p_{\mathrm{i}}^{(n+1)} \right) = \frac{\boldsymbol{\nabla} \cdot \mathbf{u}_{\mathrm{i}}^{*}}{\Delta t}, \tag{16}$$

$$\mathbf{u}_{\mathrm{i}}^{(n+1)} = \mathbf{u}_{\mathrm{i}}^{*} - \frac{1}{\rho_{\mathrm{i}}^{*}} \boldsymbol{\nabla} p_{\mathrm{i}}^{(n+1)} \Delta t, \tag{17}$$

$$\mathbf{r}_{\mathrm{i}}^{(n+1)} = \mathbf{r}_{\mathrm{i}}^{(n)} + \frac{1}{2} \left(\mathbf{u}_{\mathrm{i}}^{(n)} + \mathbf{u}_{\mathrm{i}}^{(n+1)} \right) \Delta t + \boldsymbol{\delta}\mathbf{r}_{\mathrm{i}}^{(n)}. \tag{18}$$

Boundary conditions are enforced through multiple boundary tangent (MBT) method described in [33] while first derivative and Laplace operator of vector functions are approximated through following expressions

$$\frac{\partial f_{\mathrm{i}}^{m}}{\partial x_{\mathrm{i}}^{k}} a_{\mathrm{i}}^{kl} = \sum_{\mathrm{j}} \frac{1}{\psi_{\mathrm{j}}} \left(f_{\mathrm{j}}^{m} - f_{\mathrm{i}}^{m} \right) \frac{\partial W_{\mathrm{ij}}}{\partial x_{\mathrm{i}}^{l}}, \tag{19}$$

$$\frac{\partial^2 f_{\mathrm{i}}^{m}}{\partial x_{\mathrm{i}}^{k} \partial x_{\mathrm{i}}^{k}} a_{\mathrm{i}}^{ml} = 8 \sum_{\mathrm{j}} \frac{1}{\psi_{\mathrm{j}}} \left(f_{\mathrm{i}}^{m} - f_{\mathrm{j}}^{m} \right) \frac{r_{\mathrm{ij}}^{m}}{r_{\mathrm{ij}}^{2}} \frac{\partial W_{\mathrm{ij}}}{\partial x_{\mathrm{i}}^{l}}. \tag{20}$$

Here, $a_{\mathrm{i}}^{kl} = \sum_{\mathrm{j}} \frac{r_{\mathrm{ij}}^{k}}{\psi_{\mathrm{j}}} \frac{\partial W_{\mathrm{ij}}}{\partial x_{\mathrm{i}}^{l}}$ is a corrective second rank tensor that eliminates particle inconsistencies. Left hand side of (16) is discretized as

$$\frac{\partial^2 f_{\mathrm{i}}^{m}}{\partial x_{\mathrm{i}}^{k} \partial x_{\mathrm{i}}^{k}} \left(2 + a_{\mathrm{i}}^{kk} \right) = 8 \sum_{\mathrm{j}} \frac{1}{\psi_{\mathrm{j}}} \left(f_{\mathrm{i}}^{m} - f_{\mathrm{j}}^{m} \right) \frac{r_{\mathrm{ij}}^{k}}{r_{\mathrm{ij}}^{2}} \frac{\partial W_{\mathrm{ij}}}{\partial x_{\mathrm{i}}^{k}}. \tag{21}$$

4. Problem setup and validation

The bubble is placed at a height of $h = 2r$ above the bottom wall in a rectangular computational domain with a height and a width of $H = 10r$ and $W = 6r$, respectively. No-slip boundary condition along with a potential difference of $\Delta\phi = E_{\infty}/H$ is applied to top and bottom walls while the periodicity condition is implemented on the side boundaries. In the absence of the bubble in the computational domain, the periodic boundary condition for the electric potential produces a uniform downward electric field parallel to the side boundaries. Particles discretizing the bubble are positioned along concentric circles around the bubble's center. The radii of consecutive circles differ by one particle spacing and the outermost circle's radius is equal to r. The number of particles along each of these circles vary to keep the overall inter-particle spacing

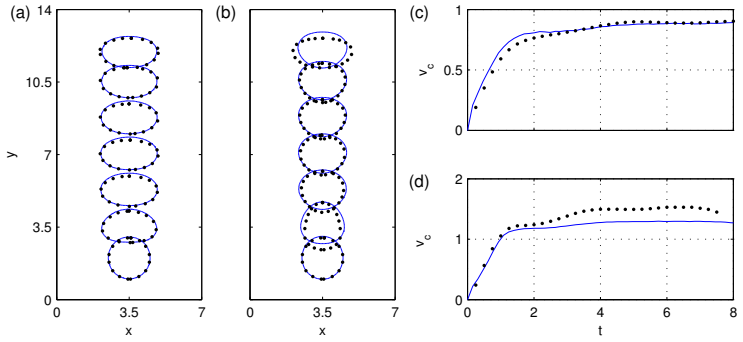

Figure 1: The comparison of the bubble shape and centroid velocities for non-electrified (a,c) and electrified (b,d) cases of the present study with Mahlmann *et al.* [15] where the solid line corresponds to the results of the current study.

uniform. Fluid particles are arranged on a uniformly spaced Cartesian grid where particles coinciding with the bubble are removed.

In our previous study [32], the in-house code and the numerical algorithm used in this study were extensively validated via comparing the results of bubble rising simulations with those from Hysing *et al.* [34] and Susmann *et al.* [35]. However, to present a self-contained study here, we have performed further validations through numerically simulating a bubble rising problem with and without electric field, included in the study of Mahlmann *et al.* [15]. The dimensions of the computational domain are set to those given in [15], namely, $W = 7r$, $H = 14r$ and $h = 2r$, and all boundaries are treated as solid walls with no-slip boundary condition while as for the boundary conditions for the electric potential, the Dirichlet and Neumann boundary conditions are imposed on horizontal and vertical walls, respectively. Both cases have $\mathrm{Re} = 250$ and $\mathrm{Bo} = 1$, while the electrified case has the electrical Capillary number of $\mathrm{Ec} = 1$. Figure 1 compares the bubble shapes and centroid vertical velocities of non-electrified and electrified cases with those of Mahlmann *et al.* [15]. The results for the non-electric test case have a clear match both in terms of the bubble shape and its vertical velocity. In the electrified case, both shape and the motion of the bubble are in a satisfactory agreement with those of Mahlmann except at a stage where the bubble is close to the boundary.

In this section of the present work, the dependency of the numerical results to the particle resolution is tested. The resolution of the particles is scaled with respect to the bubble diameter; the number of particles for a unit diameter of bubble (x/d). In order to perform the test, a case with dimensionless numbers equal to $\mathrm{Re} = 400$, $\mathrm{Bo} = 12$ and $\mathrm{Ec} = 5$ is simulated for different particle resolutions. The resolution is varied from 30 x/d to 80 x/d with a unit increment of 10. Figure 2 shows the bubble centroid positions and velocities for these particle resolutions where one can observe the convergence of the solution as the particle resolution increases. The centroid position of 70 x/d and 80 x/d adequately matches, and their velocities at both the accelerating and terminal stages have negligible difference. Thus, in this study, the particle resolution of 70 x/d is used to simulate the validation and forthcoming test cases.

5. Results

The rising of a single droplet in a quiescent fluid can be modeled using four dimensionless numbers, namely the density ratio $\mathcal{D}$, the viscosity ratio $\mathcal{V}$, the Reynolds number Re and the Bond number Bo. The introduction of electric forces to the droplet rising problem adds three new dimensionless parameters to the numerical model. These parameters are electrical permittivity $\mathcal{P}$ and conductivity ratios $\mathcal{C}$, and electrical Capillary number Ec. In order to simulate the droplet rising for an oil-water system, some of these physical dimensionless parameters - density, viscosity, electrical permittivity and conductivity ratios - are set to physically proper values of $\mathcal{D} = 1.25$, $\mathcal{V} = 0.01$, $\mathcal{P} = 20$ and $\mathcal{C} = 100$. Other dimensionless parameters - Reynolds, Bond and electrical Capillary numbers - are employed to consider the various conditions of

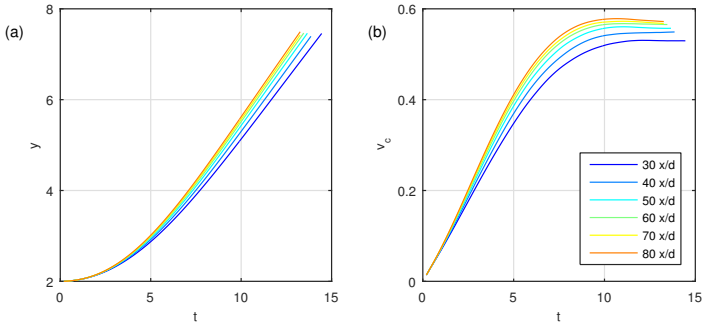

Figure 2: The temporal evolution of centroid positions and velocities of the validation test case with dimensionless parameters of Re = 400, Bo = 12 and Ec = 5 for six different particle resolutions.

Table 1: The dimensionless parameters and their corresponding magnitudes, which have been used to investigate the effect of electrical Capillary number.

Case	Re	Bo	Ec	$\mathcal{D}$	$\mathcal{V}$	$\mathcal{P}$	$\mathcal{C}$
E0	400	12	0	1.25	0.01	20	100
E1	400	12	1	1.25	0.01	20	100
E2	400	12	2	1.25	0.01	20	100
E3	400	12	3	1.25	0.01	20	100
E4	400	12	4	1.25	0.01	20	100
ERB	400	12	5	1.25	0.01	20	100

droplet rising of an oil-water system. According to the leaky dielectric model and based on the permittivity and conductivity ratios used in this paper [36], the droplet deforms prolately if the gravitational force is absent. However, the deformation of the droplet rising in the presence of gravitational and electric forces needs further investigation which is the premise of this study.

Figure 3 represents the normalized magnitudes for various force components effecting the rise of a droplet at different elevations of the simulation domain for the test case with Re = 400, Bo = 12, Ec = 5. These forces are the electric, surface tension, viscous, buoyancy, pressure and total forces illustrated by their initial letters. In order to identify the location of droplet positions shown in sub-figure (a), there are some symbols indicating the position of their center of mass that can be correlated with sub-figures (b-e). These competition of these force components will be used in the following sections to justify physical behaviour of the droplet under different conditions during its rise which will be discussed wherever appropriate.

5.1. Variations of Ec

In this section, the variation of electrical Capillary number and its impact on the droplet rising is studied. The electrical Capillary number is varied by changing the external electric field strength by means of adjusting the applied electric potential on the horizontal domain boundaries. The droplet is subjected to six different electric field strengths tabulated in table 1, and the dimensionless parameters and their magnitudes are presented therein as well. The electrical Capillary number yields the relative significance of electric and surface tension forces. In this part, the Reynolds and Bond numbers are kept constant for all test cases. Thus, the increase in the electrical Capillary number might be interpreted as the enhancement of the electric forces compared to inertia, surface tension and viscous forces.

In order to show the impact of electric forces on the droplet rising, figure 4 presents droplet shape and velocity streamlines in the half computational domain at five early instants, sorted from left to right, for $E0$ and ERB cases of table 1 shown at the top and bottom part of the figure, respectively. As can be observed from the figure, in the absence of the electric forces, the droplet rises forming an oblate shape

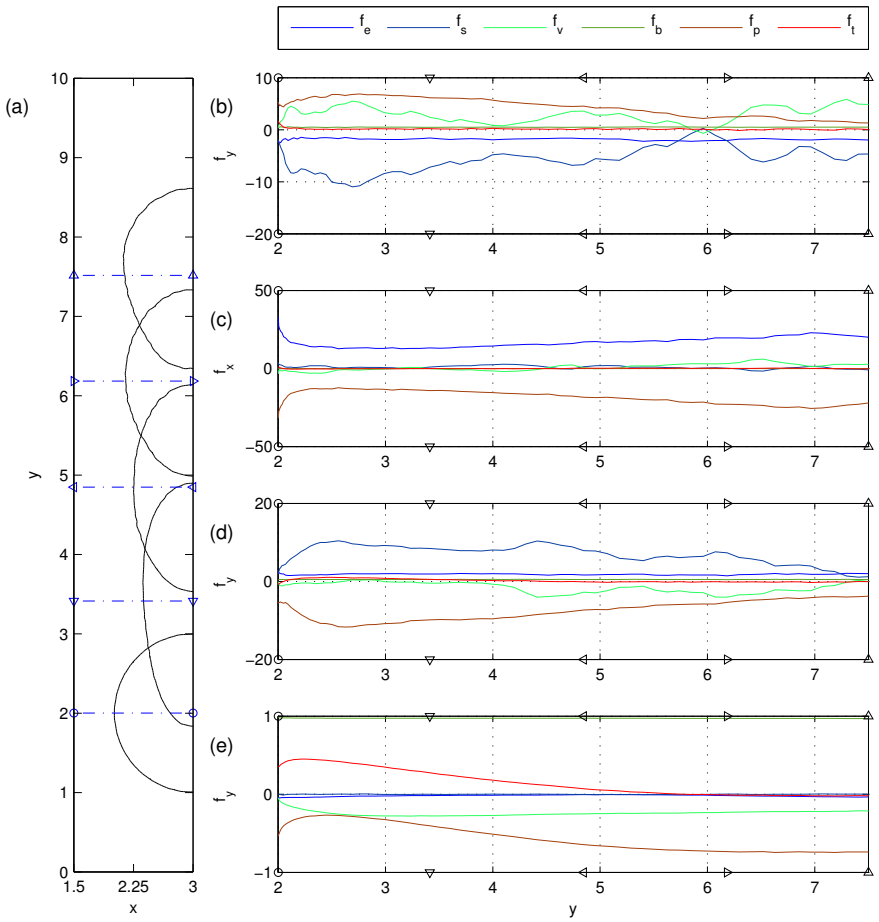

Figure 3: Comparison of various force components (f_y in sub figure b, d and f_x in sub figure c, e) for the test-case with Re = 400, Bo = 12, Ec = 5 shown in (a), at the top point (b and c) and side point of the droplet (d and e) for electric force f_e, surface tension force f_s, viscous force f_v, buoyancy force f_b, pressure gradient force f_p and total force f_t.

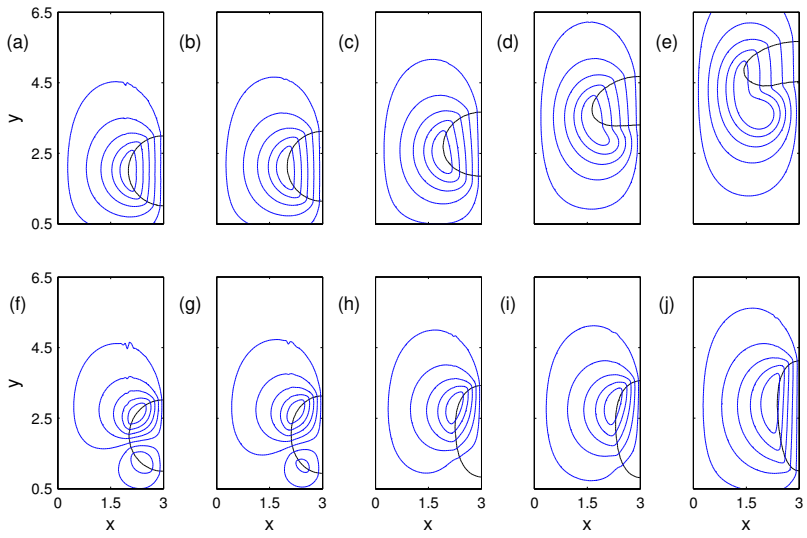

Figure 4: droplet shapes and velocity streamlines for non-electrified and electrified cases at five early instants of the rising; The upper row shows the non-electrified case $E0$ at (a) $t = 0.4$, (b) $t = 10$, (c) $t = 5$, (d) $t = 9$ and (e) $t = 13$ while the bottom one represents the electrified case ERB, at (f) $t = 0.4$, (g) $t = 1$, (h) $t = 2$, (i) $t = 2.4$ and (j) $t = 4$.

due to the hydrodynamic drag at the droplet front. However, the application of a sufficiently large electric force elongates the droplet prolately. Considering the vortex formation for the $E0$ case, a single vortex is generated at the sides of the droplet at the early instances of the rising, but the vortex gradually moves towards the region behind the droplet. This induces an upward jet current of the surrounding fluid beneath the droplet, which promotes the formation of an oblate shape. As for the case of ERB, a pair of vortices is generated due to the electric forces [37]. The flow direction for these vortices can be determined by the comparison of conductivity and permittivity ratios. Based on the parameter setup of this study, these vortices encourage the droplet to elongate into the prolate shape at the early rising moments where the buoyancy effects are not significant. As the droplet ascends, the bottom vortex loses its strength due the magnification of hydrodynamic forces and finally disappears. Simultaneously, the upper vortex grows and develops at the sides of the droplet.

To quantify the deformation of a droplet, we here introduce a dimensionless parameter, referred to as the Aspect ratio, $A_r = D_y/D_x$, where D_y and D_x are droplet diameters in the vertical and horizontal directions passing the droplet centroid, respectively. Figure 5-a shows the temporal evolution of the Aspect ratio for all test cases listed in table 1. The general trend of all test cases excluding the non-electric case of $E0$ demonstrates that the Aspect ratio of the droplet increases linearly, indicating that the droplet acquires a prolate shape due to the electric force. As the droplet gets slender, the pressure drag decreases while the friction drag increases, and the surface tension force becomes augmented at the poles of the droplet due to the increase in the curvature therein. After reaching a maximum value, the Aspect ratio starts decreasing non linearly and reaches a plateau. At the peak point of the aspect ratio, the pressure and viscous drags acquire closer values to each other (refer to figure 3), and then begin to increase and decrease, respectively. Stating explicitly, surface tension tends to preserve the initial circular shape of the droplet and the hydrodynamic forces try to decrease the prolate elongation through the hydrodynamic drag forces at the droplet front, and the jet current in its wake. The Aspect ratio levels off when electrical and hydrodynamics forces balance each other. The rise in the electrical Capillary number increases the Aspect ratio of the droplet at both initial and final stages of the droplet deformation.

The temporal evolution of centroid velocity of the droplet for different electrical Capillary numbers is shown in figure 5-b. It is observed that the centroid velocity of the droplet increases with the rise of Ec. Comparing the resultant forces applied to droplet due to pressure, viscous stress and electric stresses, it

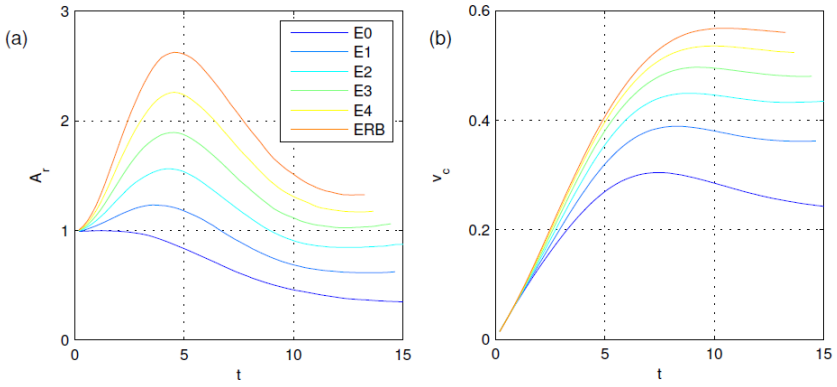

Figure 5: Temporal variations of (a) Aspect ratio A_r and (b) the centroid velocity for six different electrical Capillary number Ec in table 1.

Table 2: The dimensionless parameters and their corresponding magnitudes, which have been used to investigate the effect of Bond number.

Case	Re	Bo	Ec	$\mathcal{D}$	$\mathcal{V}$	$\mathcal{P}$	$\mathcal{C}$
B1	400	2	5	1.25	0.01	20	100
B2	400	4	5	1.25	0.01	20	100
B3	400	6	5	1.25	0.01	20	100
B4	400	8	5	1.25	0.01	20	100
B5	400	10	5	1.25	0.01	20	100
ERB	400	12	5	1.25	0.01	20	100

is seen that the electric component is one order of magnitude smaller than viscous and pressure components. However, the electric forces implicitly affect the rising velocity by changing the droplet shape (figure 4). Applying the electric field makes the droplet more slender/prolate, reducing the pressure drag while increasing the friction drag. Comparing the two drag components of cases $E0$ and ERB, it is seen that applying electric field in ERB reduces the pressure drag to approximately one third of that of $E0$ while about doubling the friction drag. The resultant drag is much less than when no electric field is applied, increasing the rise velocity of the droplet.

5.2. Variations of Bo

In this section, the influence of Bond number on the evolution of the droplet under electric field is studied in order to investigate the significance of interfacial tension forces acting on the droplet. Table 2 shows the dimensionless parameters and their magnitudes used in this section. Studying the variation of Bond number may enable one to address the role of surfactants if relevant on the droplet rising in the presence of electric field.

Figure 6-a shows the variation of Aspect ratio versus time for six cases presented in table 2. One may intuitively expect that the higher the Bond number, the droplet should become more prolate since the less surface tension force (opposing to electric force) acts on the droplet interface. However, it is observed that the Aspect ratio decreases as the Bond number increases. Remember that for all test cases of this section, both Re and Ec numbers are kept constant. Therefore, the reduction in the Bond number will correlate with the increase in the surface tension. To maintain constant Ec, electric force need to be augmented, increasing the elongation of the droplet.

The temporal evolution of the centroid velocity of the droplet are presented in figure 6-b. For all the cases except for $B1$, the centroid velocities increase monotonically in time. The initial notable decrease in the centroid velocity of $B1$ is owing to the electrical interaction between the droplet and bottom boundary.

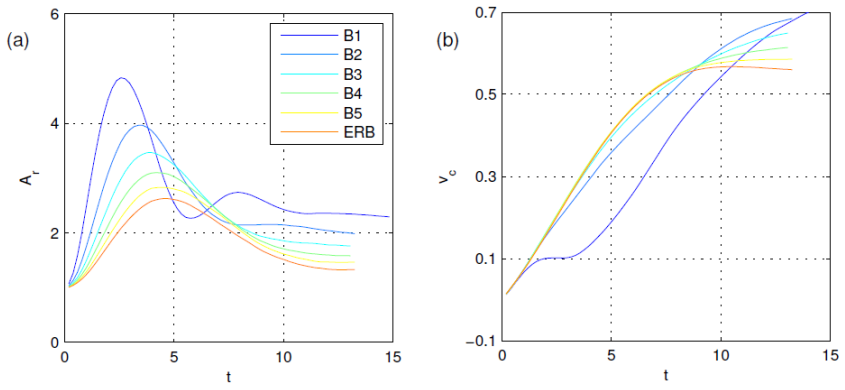

Figure 6: Temporal variations of (a) Aspect ratio A_r and (b) the centroid velocity for six different Bond numbers, namely, $B1$ - ERB; the dimensionless parameters of these cases are given in table 2.

It is observed here that the bottom boundary pulls the droplet towards itself due to the asymmetric electric force balance at the interface right after the droplet is released.

6. Conclusion

In this paper, the bubble rising is numerically investigated for an oil-water system in presence of an externally applied electric field. The leaky dielectric model is used to implement the electric forces on the system and the Continuum Surface Force (CSF) method is employed for surface tension force. The rising of a single bubble is investigated for possible influences of different electric field strengths, and changes in surface tension coefficient through the variations of electrical Capillary and Bond numbers, respectively. Afterwards, the interactions of a bubble pair are simulated for different orientations and initial center to center distances.

The general trend of bubble Aspect ratio is a linear increase to a maximum value which follows by a non-linear fashion reaching a plateau where the electric and hydrodynamic forces balance each other. Moreover, it is found that the bubble Aspect ratio increases by incrementing electrical Capillary number, and decrementing the Bond number. Decrementing the Bond number, the surface tension force is stronger on bubble interface which attempts to preserve the circular bubble shape. Since the electrical Capillary number is kept constant for variations of Bond number, the electric forces are augmented as well, resulting in an increase in Aspect ratio by decrementing the Bond number.

The study of centroid velocity of bubble for variations of electrical Capillary and Bond numbers reveals that the centroid velocities increase with increments of electric Capillary and Reynolds number. Increase in the Bond number yields in the increase of the centroid velocities in the transient stage, in contrast to the terminal stage.

References

[1] H. Y. Yoon, S. Koshizuka, Y. Oka, Direct calculation of bubble growth, departure, and rise in nucleate pool boiling, International Journal of Multiphase Flow 27 (2001) 277–298.

[2] K. Galvin, S. Pratten, N. Shankar, G. Evans, S. Biggs, D. Tunaley, Production of high internal phase emulsions using rising air bubbles, Chemical engineering science 56 (2001) 6285–6293.

[3] B. S. Murray, E. Dickinson, Y. Wang, Bubble stability in the presence of oil-in-water emulsion droplets: Influence of surface shear versus dilatational rheology, Food Hydrocolloids 23 (2009) 1198–1208.

[4] T. Takahashi, T. Miyahara, Y. Nishazaki, Separation of oily water by bubble column., journal of chemical engineering of Japan 12 (1979) 394–399.

[5] A. Al-Shamrani, A. James, H. Xiao, Separation of oil from water by dissolved air flotation, Colloids and Surfaces A: Physicochemical and Engineering Aspects 209 (2002) 15–26.

[6] F. Pigeonneau, Mass transfer of a rising bubble in molten glass with instantaneous oxidation–reduction reaction, Chemical Engineering Science 64 (2009) 3120–3129.
[7] R. Clift, J. Grace, M. Weber, Bubbles, drops and particles, Vol. 5. Nos. 1-4, 1988 Modelling of Three Phase Sparged Catalytic Reactors 5 (1978).
[8] B. Cuenot, J. Magnaudet, B. Spennato, The effects of slightly soluble surfactants on the flow around a spherical bubble, Journal of Fluid Mechanics 339 (1997) 25–53.
[9] R. B. Fdhila, P. Duineveld, The effect of surfactant on the rise of a spherical bubble at high reynolds and peclet numbers, Physics of Fluids (1994-present) 8 (1996) 310–321.
[10] D. Rodrigue, D. De Kee, C. C. M. Fong, An experimental study of the effect of surfactants on the free rise velocity of gas bubbles, Journal of non-newtonian fluid mechanics 66 (1996) 213–232.
[11] D. Dey, J. Boulton-Stone, A. Emery, J. Blake, Experimental comparisons with a numerical model of surfactant effects on the burst of a single bubble, Chemical engineering science 52 (1997) 2769–2783.
[12] T. L. Metcalfe, P. J. Dillon, C. D. Metcalfe, Detecting the transport of toxic pesticides from golf courses into watersheds in the precambrian shield region of ontario, canada, Environmental Toxicology and Chemistry 27 (2008) 811–818.
[13] E. Emmanuel, K. Hanna, C. Bazin, G. Keck, B. Clément, Y. Perrodin, Fate of glutaraldehyde in hospital wastewater and combined effects of glutaraldehyde and surfactants on aquatic organisms, Environment international 31 (2005) 399–406.
[14] G. Taylor, Studies in electrohydrodynamics. i. the circulation produced in a drop by electrical field, in: Proceedings of the Royal Society of London A: Mathematical, Physical and Engineering Sciences, volume 291, The Royal Society, pp. 159–166.
[15] S. Mählmann, D. T. Papageorgiou, Buoyancy-driven motion of a two-dimensional bubble or drop through a viscous liquid in the presence of a vertical electric field, Theoretical and Computational Fluid Dynamics 23 (2009) 375–399.
[16] Q. Yang, B. Q. Li, J. Shao, Y. Ding, A phase field numerical study of 3d bubble rising in viscous fluids under an electric field, International Journal of Heat and Mass Transfer 78 (2014) 820–829.
[17] R. A. Gingold, J. J. Monaghan, Smoothed particle hydrodynamics: theory and application to non-spherical stars, Monthly notices of the royal astronomical society 181 (1977) 375–389.
[18] J. J. Monaghan, Simulating free surface flows with sph, Journal of computational physics 110 (1994) 399–406.
[19] S. Shao, E. Y. Lo, Incompressible sph method for simulating newtonian and non-newtonian flows with a free surface, Advances in Water Resources 26 (2003) 787–800.
[20] J. Monaghan, A. Kocharyan, Sph simulation of multi-phase flow, Computer Physics Communications 87 (1995) 225–235.
[21] X. Hu, N. A. Adams, An incompressible multi-phase sph method, Journal of computational physics 227 (2007) 264–278.
[22] A. Rahmat, N. Tofighi, M. Shadloo, M. Yildiz, Numerical simulation of wall bounded and electrically excited rayleigh-taylor instability using incompressible smoothed particle hydrodynamics, Colloids and Surfaces A: Physicochemical and Engineering Aspects 460 (2014) 60–70.
[23] N. Tofighi, M. Ozbulut, A. Rahmat, J. Feng, M. Yildiz, An incompressible smoothed particle hydrodynamics method for the motion of rigid bodies in fluids, Journal of Computational Physics 297 (2015) 207–220.
[24] C. Antoci, M. Gallati, S. Sibilla, Numerical simulation of fluid–structure interaction by sph, Computers & Structures 85 (2007) 879–890.
[25] J. Brackbill, D. Kothe, C. Zemach, A continuum method for modeling surface-tension, J. Comput. Phys. 100 (1992) 335–354.
[26] D. A. Saville, Electrohydrodynamics: The Taylor-Melcher leaky dielectric model, Annual Review of Fluid Mechanics 29 (1997) 27–64.
[27] J. Hua, L. K. Lim, C.-H. Wang, Numerical simulation of deformation/motion of a drop suspended in viscous liquids under influence of steady electric fields, Physics of Fluids (1994-present) 20 (2008) 113302.
[28] J. J. Monaghan, J. C. Lattanzio, A refined particle method for astrophysical problems, Astronomy and Astrophysics 149 (1985) 135–143.
[29] J. J. Monaghan, A. Kocharyan, SPH simulation of multiphase flow, Computer Physics Communications 87 (1995) 225–235.
[30] J. P. Morris, Simulating surface tension with smoothed particle hydrodynamics, Int. J. Numer. Methods Fluids 33 (2000) 333–353.
[31] N. Tofighi, M. Yildiz, Numerical simulation of single droplet dynamics in three-phase flows using ISPH, Comput. Math. Appl. 66 (2013) 525–536.
[32] A. Zainali, N. Tofighi, M. S. Shadloo, M. Yildiz, Numerical investigation of newtonian and non-newtonian multiphase flows using isph method, Computer Methods in Applied Mechanics and Engineering 254 (2013) 99–113.
[33] M. Yildiz, R. A. Rook, A. Suleman, SPH with the multiple boundary tangent method, Int. J. Numer. Methods Eng. 77 (2009) 1416–1438.
[34] S. Hysing, S. Turek, D. Kuzmin, N. Parolini, E. Burman, S. Ganesan, L. Tobiska, Quantitative benchmark computations of two-dimensional bubble dynamics, International Journal for Numerical Methods in Fluids 60 (2009) 1259–1288.
[35] M. Sussman, P. Smereka, S. Osher, A level set approach for computing solutions to incompressible two-phase flow, Journal of Computational physics 114 (1994) 146–159.
[36] A. Rahmat, N. Tofighi, M. Yildiz, Numerical simulation of the electrohydrodynamic effects on bubble rising using the sph method, International Journal of Heat and Fluid Flow 62 (2016) 313–323.
[37] M. Shadloo, A. Rahmat, M. Yildiz, A smoothed particle hydrodynamics study on the electrohydrodynamic deformation of a droplet suspended in a neutrally buoyant newtonian fluid, Computational Mechanics 52 (2013) 693–707.